Available online at www.sciencedirect.com
ScienceDirect
Trans. Nonferrous Met. Soc. China 35(2025) 3778−3794
Transactions of Nonferrous Metals Society of China
www.tnmsc.cn

Improved unified dislocation density-based constitutive model for high-temperature deformation and dynamic recrystallization behaviors of GH4698 superalloy

Pei-zhi YAN[1], Dong-xu WEN[1], Qi-feng DING[1], Liang HUANG[1], Xiao-li YANG[2], Zhi-cheng ZHANG[2], Jian-jun LI[1,3]

1. State Key Laboratory of Materials Processing and Die & Mould Technology, School of Materials Science and Engineering, Huazhong University of Science and Technology, Wuhan 430074, China;
2. Daye Special Steel Co., Ltd., Huangshi 435001, China;
3. Hubei Huangshi Kechuang Mold Technology Research Institute Co., Ltd., Huangshi 435007, China

Received 12 March 2024; accepted 14 November 2024

Abstract: The high-temperature deformation and dynamic recrystallization (DRX) behaviors of GH4698 superalloy were investigated via hot compression tests, and an improved unified dislocation density-based constitutive model was established. The results indicate that with the temperature decreasing or the strain rate increasing, the flow stress increases and the DRX fraction decreases. However, as the strain rate increases from 1 to 10 s^{-1}, rapid dislocation multiplication and deformation heat accelerate the DRX nucleation, which further increases the DRX fraction. Discontinuous DRX nucleation is the dominant DRX nucleation mechanism, and continuous DRX nucleation mainly occurs under low strain rates. For the developed improved unified dislocation density-based constitutive model, the correlation coefficient, average absolute relative error, and root mean square error between the measured and predicted stresses are 0.994, 7.32% and 10.8 MPa, respectively. Meanwhile, the correlation coefficient between the measured and predicted DRX fractions is 0.976. These indicate that the developed model exhibits high accuracy in predicting the high-temperature deformation and DRX behaviors of GH4698 superalloy.

Key words: Ni-based superalloy; constitutive model; high-temperature deformation; dynamic recrystallization

1 Introduction

Ni-based superalloys have exceptional high-temperature strength, corrosion resistance, creep resistance and fatigue resistance, which are considered as the most competitive materials for manufacturing critical components of aeroengines [1,2]. However, high deformation resistance, high forming temperature and narrow processing window increase the difficulty of processing and application of Ni-based superalloys [3]. Additionally, the high degree of alloying results in the complicated microstructure evolution and challenges in balancing multiple properties [4,5]. Therefore, it is imperative to investigate the high-temperature deformation behaviors and explore the microstructure evolution mechanism of Ni-based superalloys.

Over the last few years, extensive studies have been conducted on the high-temperature deformation behaviors of Ni-based superalloys. KUMAR et al [6] reported that the work hardening (WH) behavior of a Ni-based superalloy was highly relevant to the increase of dislocation density and the formation of subgrains. WEN et al [7] found

Corresponding author: Dong-xu WEN, Tel: +86-13517208786, E-mail: dxwen@hust.edu.cn, wendxcsu@126.com
https://doi.org/10.1016/S1003-6326(25)66912-3

that the discontinuous softening characteristic of the flow stress of FGH4113A superalloy was caused by the competition between WH and dynamic recrystallization (DRX). Many researchers have shown that the DRX nucleation mechanisms of Ni-based superalloys during high-temperature deformation mainly consist of continuous DRX nucleation and discontinuous DRX nucleation [8,9]. ZHU et al [10] concluded that the twin DRX nucleation was also one of the DRX nucleation mechanisms in Alloy 925. YAN et al [11] found that δ phase in an aging-treated Ni-based superalloy provided a preferential site for DRX nucleation, and DRX promoted the fracture of δ phase through DRXed grain growth and subgrain rotation. These studies indicate that the high-temperature deformation and DRX behaviors of Ni-based superalloys involve intricate microstructure evolution, which requires further investigation.

For the investigation of high-temperature deformation behaviors, constitutive modelling is an indispensable tool. Due to the empirical characteristics and relatively few parameters, many phenomenological constitutive models have been established to reproduce the high-temperature deformation behaviors of Ni-based superalloys, such as Arrhenius model [12], Johnson−Cook model [13] and Voce−Kocks model [14]. Artificial-neural-network constitutive models with the distinguishing feature without involving model assumptions have been used to predict the high-temperature deformation behaviors of Inconel 625 alloy [15], Alloy 925 [16] and other Ni-based superalloys [17,18]. However, the phenomenological and artificial-neural-network constitutive models are mainly established on mathematical relations without considering the physical parameters of deformation mechanisms. In contrast, the physically-based constitutive models consider physical mechanisms such as thermal activation, dislocation density evolution and softening mechanism. TANG et al [19] established a unified viscoplastic constitutive model to predict the microstructure evolution and flow behaviors of Inconel 718 alloy. HE et al [20] reproduced the flow stress of a Ni-based alloy by considering the evolution of dislocation density, subgrains and grain structure. GUO et al [21] developed a dislocation-based damage-coupled constitutive model for a single crystal superalloy to evaluate the creep life. HE et al [22] constructed a physically-based constitutive model considering the effect of μ phase to forecast the high-temperature deformation behaviors of a Ni−Mo−Cr-based superalloy. These models indicate that the prediction of high-temperature deformation and DRX behaviors of Ni-based superalloys necessitates the development of precise physically-based models due to the complicated physical mechanisms involved.

GH4698 superalloy is an aging-strengthened Ni-based superalloy with excellent comprehensive mechanical properties and durability. The three DRX nucleation mechanisms of GH4698 super-alloy have been confirmed by LI et al [23,24], i.e., discontinuous, continuous, and twin DRX nucleation. ZHANG et al [25] and CHEN et al [26] constructed Arrhenius models to reproduce the high-temperature deformation behaviors of GH4698 superalloy. CHEN et al [27] suggested that the optimal deformation parameters of GH4698 superalloy were 1010−1100 °C and 0.001−0.1 s^{-1}. These studies have laid a foundation for designing and optimizing hot forming processes and mechanical properties of GH4698 superalloy. However, there are few studies on the evolution of DRX mechanisms and the physically-based constitutive model, which needs to be further advanced.

In this work, GH4698 superalloy was firstly treated with hot compression under different deformation parameters to investigate the influence of deformation temperature and strain rate on high-temperature deformation behaviors. Subsequently, the microstructure evolution under different deformation parameters was studied through electron backscattered diffraction (EBSD) analysis, and the evolution of DRX mechanisms under different strain rates was discussed. Finally, an improved unified dislocation density-based constitutive model incorporating DRX effect was established to characterize the high-temperature deformation and DRX behaviors.

2 Experimental

The chemical compositions (wt.%) of GH4698 superalloy were as follows: Cr 14.35, Mo 2.98, Ti 2.65, Nb 2.11, Al 1.69, Fe 0.11, C 0.05, and Ni balance. A Gleeble−3500 simulation machine was applied for the hot compression test. The specimens

for the test were machined into a cylinder with dimensions of *d*8 mm×12 mm. The hot compression tests were implemented over the temperature range of 1020−1200 °C and the strain rate range of 0.001−10 s^{-1}, and the maximum true strain was controlled to be 0.9. Figure 1 illustrates the diagram of the hot compression procedure. The specimen was warmed to the set temperature and maintained for 180 s. Subsequently, the hot compression test was performed, and water quenching was carried out immediately after the test.

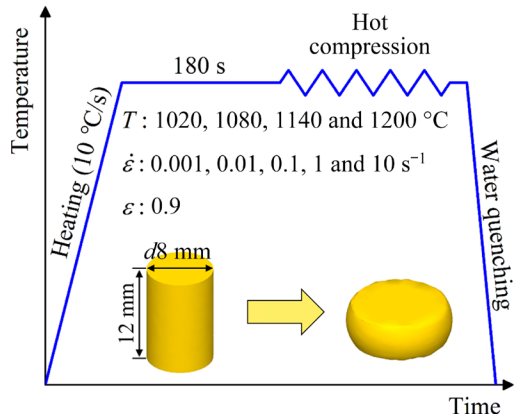

Fig. 1 Diagram of hot compression procedure

All the specimens were bisected along the compression axis by electro-discharge machining after the hot compression test. The exposed surface of the specimen was sanded with silicon carbide abrasive paper and then polished with diamond polishing paste. Optical microscope (OM) and EBSD analyses were employed for microstructure observation. For OM observation, specimens were etched for 20−50 s in the corrosive solution of HCl (50 mL), CH_3CH_2OH (100 mL) and $CuCl_2$ (10 g). Zeiss Axiolab 5 microscope was used for the OM observation. For the EBSD specimens, vibration polishing was applied to eliminating the residual stress of the surface. The EBSD analysis was performed on an FEI Quanta650 FEG FSEM machine, and the scanning area was selected as 500 μm × 500 μm with a step of 1 μm.

Figure 2 presents the metallographic image of the original uncompressed specimen. The original microstructure is the equiaxed grain structure, and several twins can be observed in the black dashed circles. Referring to the intercept method in ASTM standard (E112-13(2021)), the average grain size was measured as 44.5 μm.

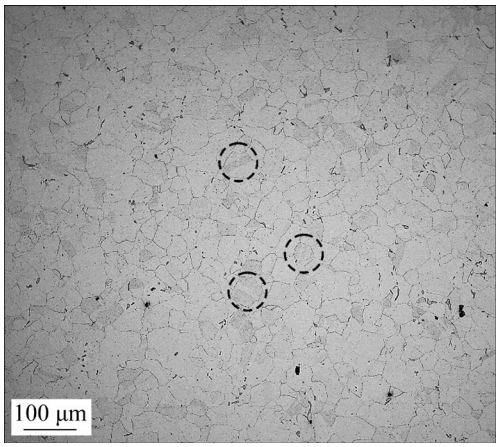

Fig. 2 Metallographic image of original uncompressed specimen

3 Results and discussion

3.1 Correction and characteristics of stress−strain curve

During the hot compression, the friction between the pressure head and the specimen results in the measured stress being higher than the actual stress. Therefore, the friction correction is applied to the measured stress. The friction correction formulas are expressed as [28]

$$\begin{cases} \dfrac{\sigma_{\mathrm{O}}}{\sigma_{\mathrm{F}}}=\dfrac{8b_0r}{h}\left\{\left[\dfrac{1}{12}+\left(\dfrac{h}{rb_0}\right)^2\right]^{3/2}-\left(\dfrac{h}{rb_0}\right)^3-\dfrac{f\mathrm{e}^{-b_0/2}}{24\sqrt{3}(\mathrm{e}^{-b_0/2}-1)}\right\} \\ f=\dfrac{(r/h)b_0}{(4/\sqrt{3})-(2b_0/3\sqrt{3})} \\ b_0=\dfrac{4(r_{\max}-r_{\mathrm{top}})h}{r(h_0-h)} \\ r=r_0\sqrt{h_0/h} \\ r_{\mathrm{top}}=\sqrt{\dfrac{3h_0}{h}r_0^2-2r_{\max}^2} \end{cases} \tag{1}$$

where σ_{O} stands for the original measured stress; σ_{F} signifies the friction-corrected stress; f represents the friction factor; b_0 stands for the barrel parameter; r_0 and h_0 represent the radius and the height of the specimen before hot compression, respectively; r and h stand for the average radius and average height of the specimen after hot compression, respectively; r_{top} and $r_{\max}$ signify the top and

maximum radii of the specimen after hot compression, respectively. According to Eq. (1), the friction-corrected stresses under different deformation parameters of GH4698 superalloy are presented in Fig. 3. The friction-corrected stresses are noticeably lower than the original measured stresses. Additionally, the effect of friction on the flow stress intensifies with the strain rate rising or the deformation temperature declining.

At the beginning of deformation, WH plays a leading role. The flow stress rises sharply, and dislocation multiplication leads to a rapid increase in dislocation density [29]. With the strain further increasing, dynamic recovery (DRV) and DRX are activated, causing the deceleration of WH. This is because the dislocation rearrangement and annihilation initiated by DRV and DRX slow down the increase of dislocation density [30]. When the peak stress arrives, DRV and DRX play a dominant role, and the flow stress begins to decline [31]. As illustrated in Fig. 3, the deformation parameters exert a substantial influence on the flow stress. It is noticeable that as the deformation temperature increases, the flow stress declines. Under high deformation temperatures, the grain boundary migration and dislocation movement are facilitated, accelerating DRV and DRX [22]. Consequently, the dislocation rearrangement and annihilation are strengthened, and the dislocation density is reduced, inducing the decrease of flow stress. Besides, it indicates that as the strain rate rises, the flow stress increases. The main reason is that high strain rates cannot provide enough time for DRV and DRX. As a result, the influence of WH is significant, and the flow stress is high under high strain rates.

As illustrated in Fig. 3, the flow stress presents distinct softening characteristics after the peak stress under the strain rates of 0.001, 0.01 and 0.1 s^{-1}, which are known as the single-peak behaviors. With the strain rate rising to 1 s^{-1}, the flow stress exhibits slight softening and even continuous hardening characteristics. However, as the strain rate increases to 10 s^{-1}, the flow stress presents notable softening characteristics again, which shows single-peak behaviors under low deformation temperatures and multiple-peak behaviors under high deformation temperatures [32]. Reappearance of notable softening characteristics is

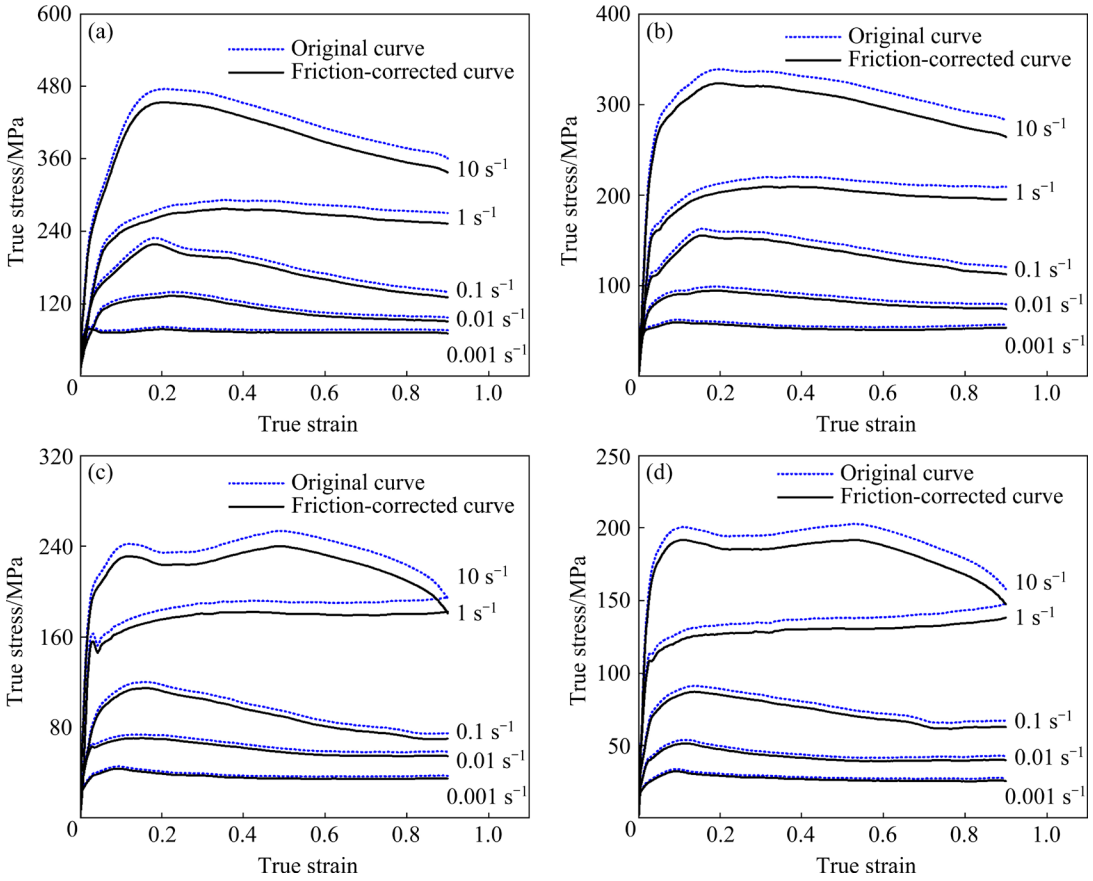

Fig. 3 Original and friction-corrected stress−strain curves of GH4698 superalloy under different deformation temperatures: (a) 1020 °C; (b) 1080 °C; (c) 1140 °C; (d) 1200 °C

because the deformation heat is difficult to diffuse fully under high strain rates, which results in the high temperature rise and adiabatic heating softening. The temperature rise can be determined by [28]

$$\begin{cases} \Delta T = \dfrac{0.95\eta}{\rho_s C_p}\int_0^{\varepsilon}\sigma_F \mathrm{d}\varepsilon \\ \eta = \begin{cases} 0\,, \dot{\varepsilon} \le 0.001\ \mathrm{s}^{-1} \\ 0.95 + 0.316\lg\dot{\varepsilon}\,, 0.001\ \mathrm{s}^{-1} < \dot{\varepsilon} < 1\ \mathrm{s}^{-1} \\ 0.95\,, \dot{\varepsilon} \ge 1\ \mathrm{s}^{-1} \end{cases} \end{cases} \tag{2}$$

where ΔT signifies the temperature change, η stands for the adiabatic correction factor, ρ_s represents the density, C_p signifies the specific heat capacity, ε signifies the strain, and $\dot{\varepsilon}$ represents the strain rate. The calculation results of temperature change are presented in Fig. 4. It demonstrates that the temperature change increases with the deformation temperature declining or the strain rate rising. The raised strain rate aggravates the temperature rising, and further enhances DRX. Meanwhile, increasing strain rate also intensifies the effect of WH [33]. Under the strain rate of 1 s^{-1}, the dynamic softening caused by DRX is difficult to counteract the enhanced WH, leading to the continuous hardening characteristics in flow stress. When the strain rate increases to 10 s^{-1}, high temperature rising significantly promotes the development of DRX, which results in notable softening characteristics in the flow stress.

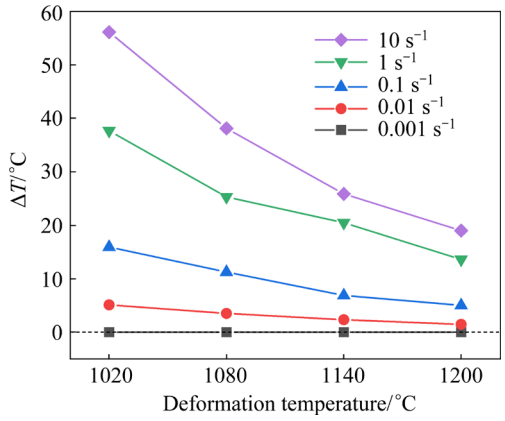

Fig. 4 Temperature change (ΔT) of GH4698 superalloy under different deformation temperatures

3.2 Microstructure evolution and DRX nucleation mechanism

To study the influence of strain rate on microstructure evolution, the inverse pole figures (IPFs) of GH4698 superalloy under different strain rates are analyzed, as illustrated in Figs. 5(a−d). Under the strain rate of 0.01 s^{-1}, most of the initial grains disappear, and the DRXed grains become the major part. The DRX fraction is measured to be 97.2%. With the strain rate increasing to 1 s^{-1}, the proportion of the initial deformed grains increases, and the DRX fraction decreases from 97.2% to 90.3% and then to 56.2%, as demonstrated in Figs. 5(a−c). This is because the deformation time is shortened under high strain rates, inducing insufficient nucleation and growth of DRXed grains and low DRX fraction. However, with the strain rate increasing to 10 s^{-1}, the DRX fraction increases to 81.3%, as illustrated in Fig. 5(d). The main reason for this change is that the temperature rise is relatively high under the strain rate of 10 s^{-1} (in Fig. 4), which advances the nucleation of DRXed grains greatly in a short deformation time. This phenomenon aligns with the previous analysis of flow softening under the strain rate of 10 s^{-1}. Figure 6(a) depicts the frequency distribution of grain boundary misorientation angle (θ) under different strain rates. As the strain rate increases from 0.01 to 10 s^{-1}, the average misorientation angle ($\overline{\theta}$) declines from 42.69° to 32.16° and then rises to 41.33°. To further analyze the evolution of grain boundaries, the corresponding variations of low-angle grain boundary (2°<θ≤10°, LAGB), medium-angle grain boundary (10°<θ≤15°, MAGB) and high-angle grain boundary (15°<θ<65°, HAGB) are illustrated in Fig. 6(b). The frequency of LAGBs increases from 8.7% to 31.3% and then decreases to 10.7%, while the frequency of HAGBs decreases from 89.9% to 66.9% and then increases to 87.9%, which is in line with the trend of DRX fraction. This is because the short deformation time is insufficient for the dislocation rearrangement and annihilation under high strain rates, which inhibits the evolution of subgrains to DRXed grains and the transformation of LAGBs to HAGBs. Nevertheless, as the strain rate increases to 10 s^{-1}, high temperature rising significantly accelerates the grain boundary migration. Moreover, under the strain rate of 10 s^{-1}, the rapid dislocation multiplication accelerates the local dislocation density to reach the critical dislocation density for DRX. Ultimately, these factors facilitate the nucleation of the DRXed grains and increase the frequency of HAGBs.

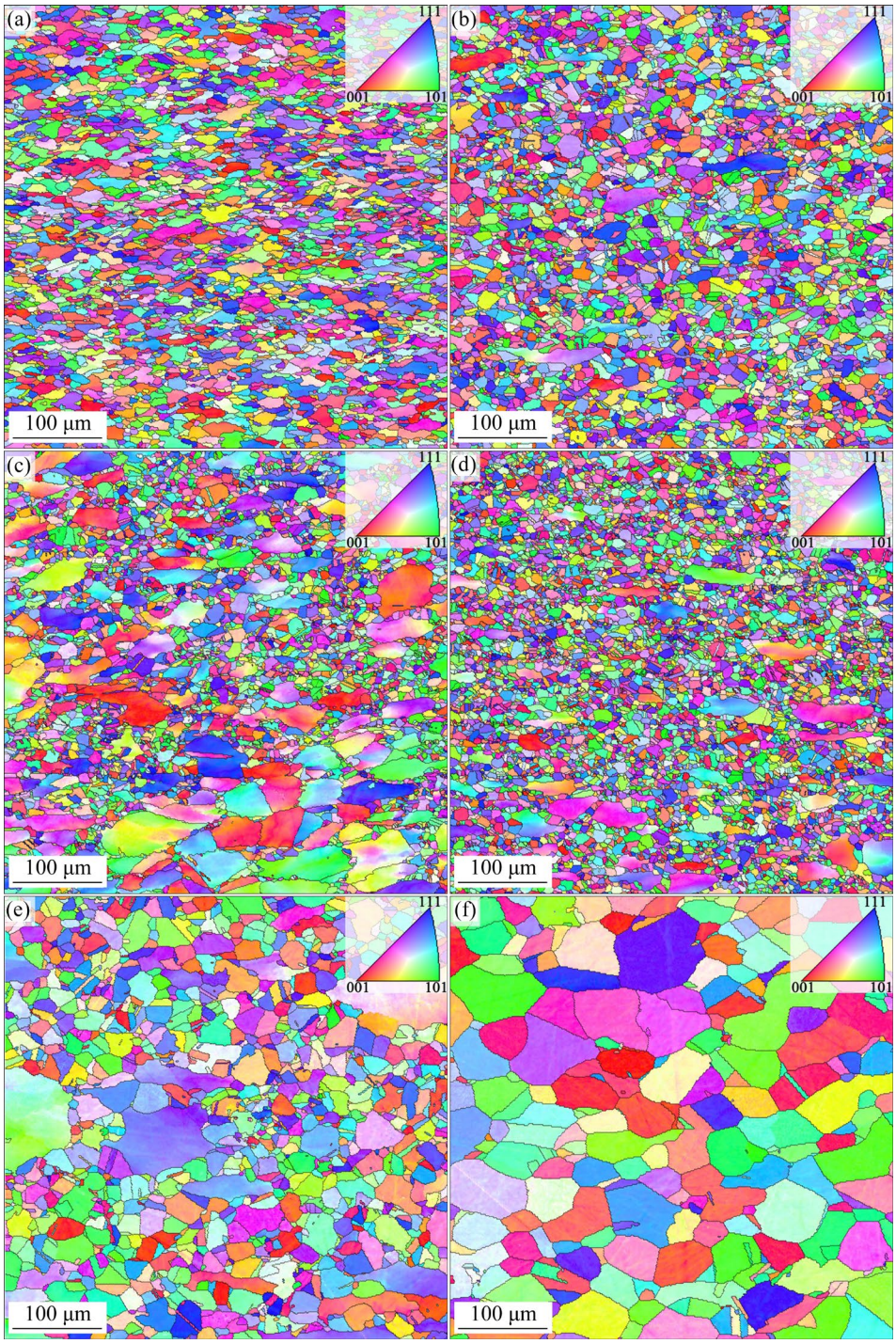

Fig. 5 IPFs of GH4698 superalloy under different deformation parameters: (a) 1020 °C, 0.01 s^{-1}; (b) 1020 °C, 0.1 s^{-1}; (c) 1020 °C, 1 s^{-1}; (d) 1020 °C, 10 s^{-1}; (e) 1080 °C, 0.1 s^{-1}; (f) 1140 °C, 0.1 s^{-1}

To investigate the influence of deformation temperature on microstructure evolution, Figs. 5(b), (e) and (f) depict the IPFs of GH4698 superalloy under different deformation temperatures. With the deformation temperature increasing from 1020 to 1140 °C, the DRX fraction increases from 90.3% to 91.8% and eventually to 96.2%. This results from the fact that the high deformation temperatures enhance the grain boundary mobility and encourage the nucleation and growth of the DRXed grains. Figure 6(c) demonstrates the distribution of grain boundary misorientation angle under different deformation temperatures. The average misorientation angle increases from 37.04° to 39.44°. Further

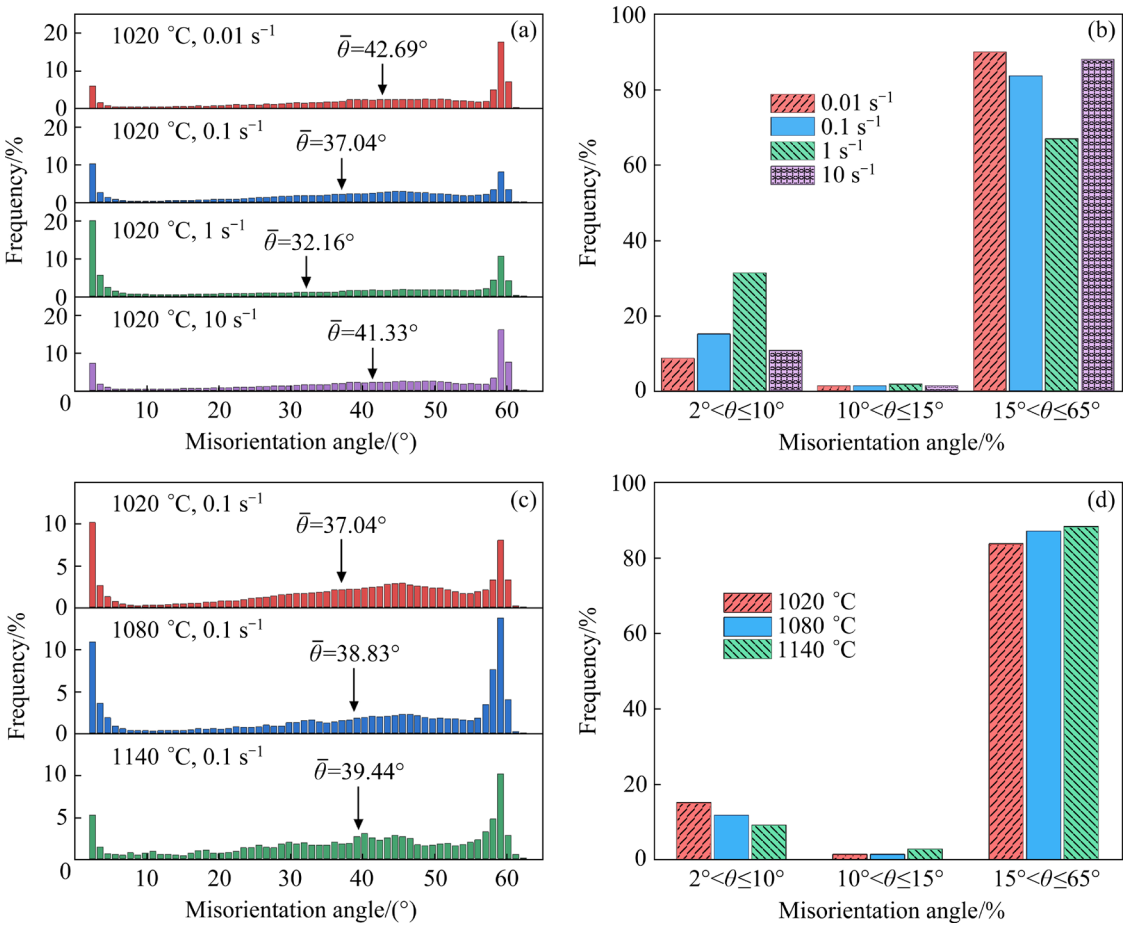

Fig. 6 Distribution of grain boundary misorientation orientation angle of GH4698 superalloy under different strain rates (a, b) and deformation temperatures (c, d)

analysis of the evolution of grain boundaries under different deformation temperatures is depicted in Fig. 6(d). With the increase of deformation temperature, the frequency of LAGBs decreases from 15.1% to 9.1%, and the frequency of HAGBs increases from 83.5% to 88.1%. The reason for the changes is that as the deformation temperature increases, subgrains and dislocation substructures gradually develop into DRXed grains, and LAGBs evolve into HAGBs.

Figures 7(a), (d) and (g) demonstrate the kernel average misorientation (KAM) maps under the deformation temperature of 1020 °C and different strain rates. The KAM angle changing from 0° to 5° corresponds to the dislocation density varying from low to high. The average KAM angles are 0.684°, 1.003° and 0.707° under the strain rates of 0.1, 1 and 10 s^{-1}, respectively. It is noted that the DRXed grains are marked as blue due to low dislocation density, and the dislocation density within deformed grains is relatively high. Figures 7(b), (e) and (h) depict the KAM maps and IPFs of selected specific grains (marked in white boxes of Figs. 7(a), (d) and (g), respectively), and the corresponding variations of intragranular misorientation angle along the measurement directions in Figs. 7(b), (e) and (h) are demonstrated in Figs. 7(c), (f) and (i), respectively. As illustrated in Figs. 7(c) and (f), the point-to-origin (PTO) misorientation angles along $L1$ and $L3$ both exceed 15°, and the peaks of point-to-point (PTP) misorientation angles along $L1$ and $L3$ above 3° can be found, signifying the large orientation gradient and the formation of substructures along the grain boundary. Furthermore, there exist the grain boundary bulging and the subgrains along grain boundaries in the selected grains of Figs. 7(b) and (e), which is consistent with the archetypal characteristics of discontinuous DRX nucleation [34]. Besides, the PTO misorientation angles along $L2$ and $L4$ exceed 13°, and this large orientation gradient denotes the lattice rotation within the deformed grains.

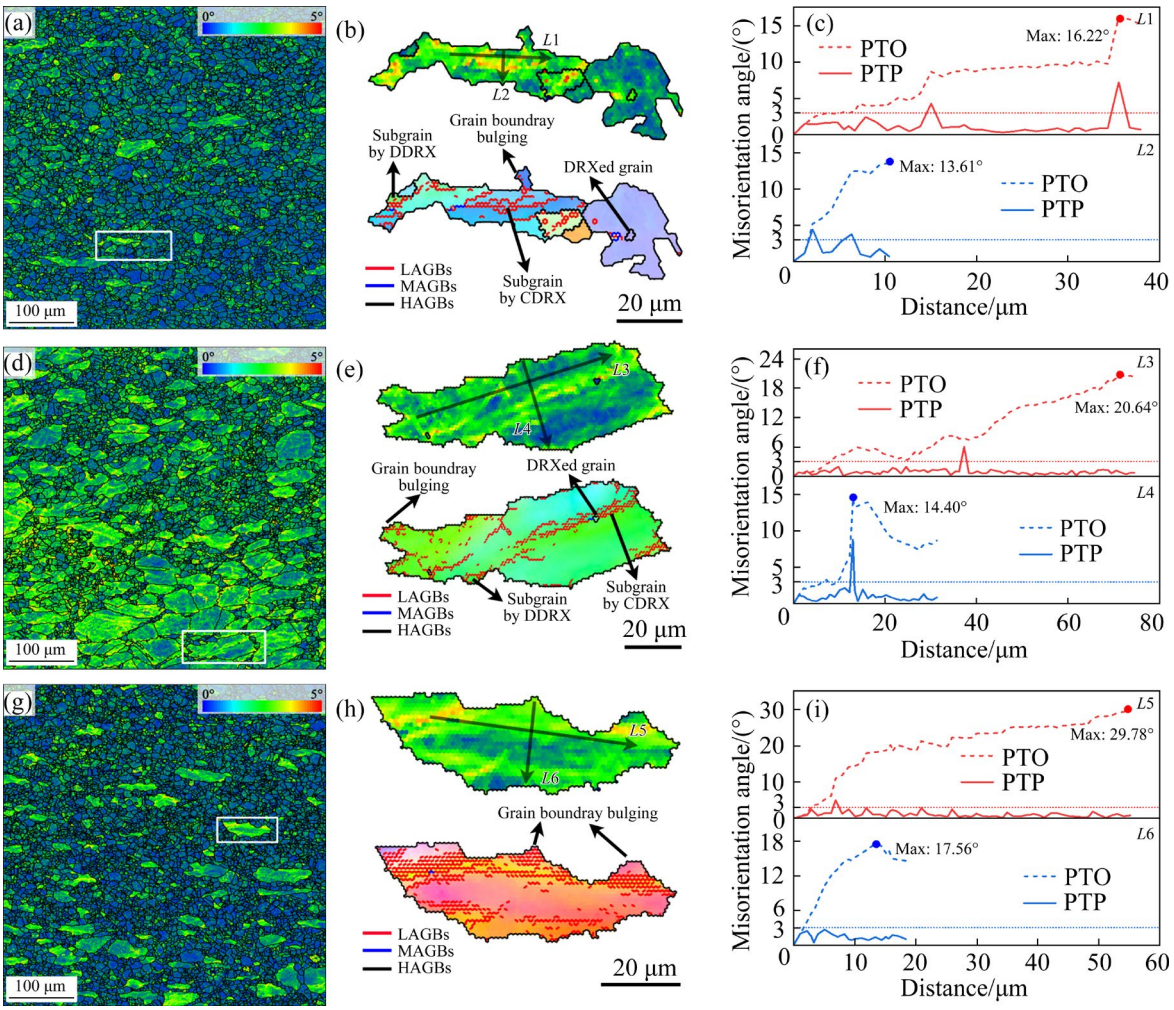

Fig. 7 KAM maps of matrix (a, d, g), KAM maps and IPFs of selected grains (b, e, h), and distribution of intragranular misorientation angle (c, f, i) along measurement directions marked in (b, e, h) under different deformation parameters: (a, b, c) 1020 °C, 0.1 s^{-1}; (d, e, f) 1020 °C, 1 s^{-1}; (g, h, i) 1020 °C, 10 s^{-1}

Meanwhile, the peaks of PTP misorientation angle curves exceed 3°, indicating the formation of substructures within the grain due to lattice rotation. Moreover, the DRXed grains and subgrains within the grains can be identified in Figs. 7(b) and (e). These phenomena confirm the existence of continuous DRX nucleation [35]. Therefore, discontinuous DRX nucleation and continuous DRX nucleation are the dominant DRX nucleation mechanisms of GH4698 superalloy during the high-temperature deformation. In addition, the PTO and PTP misorientation angles along *L5* in Fig. 7(i) exceed 20° and 3°, respectively. The grain boundary bulging and densely distributed LAGBs along the grain boundary are clearly observed in Fig. 7(h), indicating the occurrence of discontinuous DRX nucleation under the strain rate of 10 s^{-1}. Despite the high value of PTO misorientation angle along *L6*, the misorientation angle of the PTP curve is below 3°, as shown in Fig. 7(i). This implies that the formation of subgrains is inhibited under the strain rate of 10 s^{-1}, inducing the slow development of continuous DRX nucleation.

3.3 Establishment of improved unified dislocation density-based constitutive model

The evolution of dislocation density plays a critical role during high-temperature deformation of GH4698 superalloy. Due to the competition between the dislocation multiplication and dislocation annihilation, the flow stress of GH4698 superalloy exhibits pronounced WH and DRX behaviors. The classical dislocation density theory describes WH and DRV well [36]. However, the

stacking fault energy of GH4698 superalloy is low, signifying the slow development of DRV [37]. Moreover, DRX is a non-negligible mechanism for GH4698 superalloy. Therefore, the dislocation density-based model needs to be modified to incorporate the influence of WH, DRV and DRX on the flow stress.

It is assumed that three different stress terms contribute to the variation of flow stress, which are the stress for dislocation slip activation (σ_y), the stress for the dislocation substructure interaction (σ_i) and the stress for the evolution of grain size (σ_g). Therefore, the flow stress can be denoted by

$$\sigma=\sigma_y+\sigma_i+\sigma_g \tag{3}$$

The details of each stress term will be discussed in the subsequent sections.

3.3.1 Modeling σ_y

The stress for dislocation slip activation σ_y is the critical stress to start dislocation slip, which can be approximated by the yield stress. It can be taken as the corresponding stress to the 0.2% offset strain in the stress−strain curve. The stress for dislocation slip activation is linked to deformation temperature and strain rate, thus complying with the Arrhenius-type relationship, which is [18]

$$\sigma_y=A_y\dot{\varepsilon}^{n_y}\exp[Q_y/(RT)] \tag{4}$$

where T stands for the deformation temperature; R stands for the molar gas constant and equals 8.314 J/(mol·K); A_y, n_y and Q_y represent the material constants, respectively. Taking the natural logarithm of Eq. (4), the values of A_y, n_y and Q_y can be calculated by fitting the data of $\ln\sigma_y-\ln\dot{\varepsilon}$ and $\ln\sigma_y-1/T$, as illustrated in Fig. 8. The average values of A_y, n_y and Q_y are 0.07053, 0.1814 and 78.52 kJ/mol, respectively. The expression of the stress for dislocation slip activation is

$$\sigma_y=0.07053\dot{\varepsilon}^{0.1814}\exp\left(\frac{7.852\times10^4}{RT}\right) \tag{5}$$

3.3.2 Modeling σ_i

As the applied stress increases and exceeds the stress σ_y, the dislocation slip is activated, and the high-temperature deformation enters the plastic stage. Kocks−Mecking model suggests that the variations of flow stress in the plastic stage are closely related to the dislocation substructure interaction, and expression of stress for the dislocation substructure interaction is given as [38]

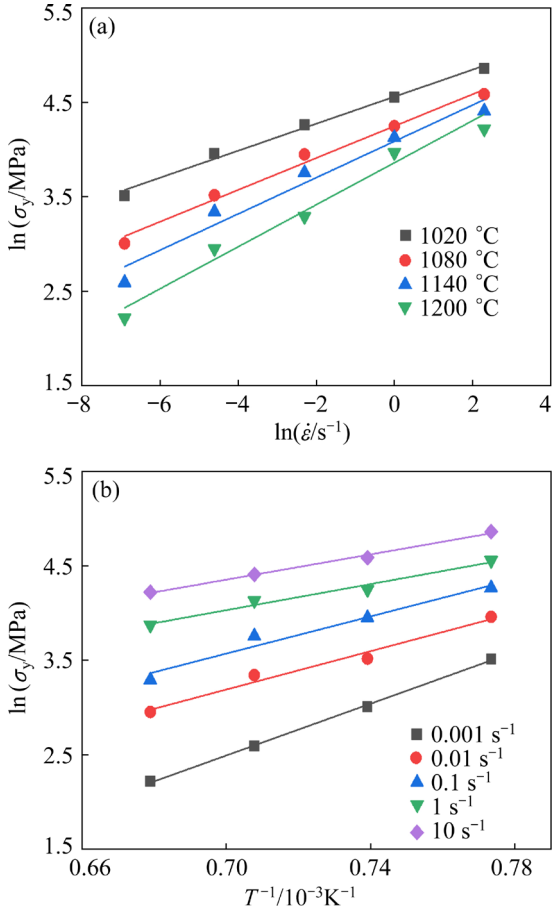

Fig. 8 Fitting lines of $\ln\sigma_y-\ln\dot{\varepsilon}$ (a) and $\ln\sigma_y-1/T$ (b) for GH4698 superalloy

$$\sigma_i=M\alpha\mu b\sqrt{\rho} \tag{6}$$

where ρ signifies the mean dislocation density, M stands for the Taylor factor and takes 3.06 for FCC structure [38], α signifies the Taylor constant and takes 0.3 [39], μ stands for the shear modulus and equals $-0.027T+86.94$ (GPa) [40], and b signifies the magnitude of Burgers vector and equals 2.54×10^{-10} m [41]. The degree of dislocation substructure interaction greatly determines the evolution of dislocation density. The rate of dislocation density evolution gives

$$\dot{\rho}=\dot{\rho}_{WH}-\dot{\rho}_{DRV}-\dot{\rho}_{DRX} \tag{7}$$

where $\dot{\rho}$ stands for the rate of dislocation density evolution. $\dot{\rho}_{WH}$, $\dot{\rho}_{DRV}$ and $\dot{\rho}_{DRX}$ represent WH, DRV and DRX terms affecting the evolution of dislocation density, respectively.

(1) Modeling $\dot{\rho}_{WH}$

The WH term $\dot{\rho}_{WH}$ is correlated with the strain rate and the mean free path (MFP) of dislocation, which is expressed as [42]

$$\dot{\rho}_{\mathrm{WH}}=\frac{M}{b\Lambda}\dot{\varepsilon} \tag{8}$$

where Λ represents the MFP of dislocation. The MFP of dislocation is strongly associated with the substructure size and the grain size, and the expression gives

$$\frac{1}{\Lambda}=\frac{1}{s}+\frac{1}{d} \tag{9}$$

where s and d signify the substructure size and the average grain size, respectively. The expressions are as follows:

$$s=f_{\mathrm{w}}/\sqrt{\rho} \tag{10}$$

$$d=Xd_{\mathrm{drx}}+(1-X)d_0 \tag{11}$$

where f_{w} represents the WH coefficient, X stands for the DRX fraction, d_{drx} signifies the DRXed grain size, and d_0 represents the initial grain size. The DRX fraction (X) is represented by [43]

$$X=1-\exp\left(-f_{\mathrm{k}}\left(\frac{\varepsilon-\varepsilon_{\mathrm{c}}}{\varepsilon_{0.5}-\varepsilon_{\mathrm{c}}}\right)^{f_{\mathrm{d}}}\right)\quad(\varepsilon\geq\varepsilon_{\mathrm{c}}) \tag{12}$$

where ε signifies the strain, f_{k} represents the DRX fraction coefficient, f_{d} stands for the DRX fraction index, ε_{c} signifies the critical strain for DRX, and $\varepsilon_{0.5}$ stands for the strain for the DRX fraction of 50%. The nucleation and growth of DRXed grains are markedly affected by deformation temperature and strain rate, and therefore Arrhenius-type relationship is applied to expressing the DRXed grain size as follows:

$$d_{\mathrm{drx}}=A_{\mathrm{ddrx}}\dot{\varepsilon}^{n_{\mathrm{ddrx}}}\exp\left(-\frac{Q_{\mathrm{ddrx}}}{RT}\right) \tag{13}$$

where A_{ddrx}, n_{ddrx} and Q_{ddrx} stand for material constants. The values of d_{drx} under different deformation parameters can be identified from metallographic images by the intercept method. Each constant can be calculated by fitting the data of $\ln d_{\mathrm{drx}}-\ln\dot{\varepsilon}$ and $\ln d_{\mathrm{drx}}-1/T$, as presented in Fig. 9. The average values of A_{ddrx}, n_{ddrx} and Q_{ddrx} are 4.196, −0.1847 and 141.9 kJ/mol, respectively. The DRXed grain size is described as

$$d_{\mathrm{drx}}=4.196\dot{\varepsilon}^{-0.1847}\exp\left(-\frac{1.419\times10^5}{RT}\right) \tag{14}$$

(2) Modeling $\dot{\rho}_{\mathrm{DRV}}$

For FCC metals, the dislocation cross-slip under low-medium deformation temperatures and the dislocation climb under high deformation temperatures are the two dominant DRV mechanisms, both resulting in the decrease of average dislocation density during deformation. The rate of dislocation density evolution caused by DRV gives [38]

$$\dot{\rho}_{\mathrm{DRV}}=f_{\mathrm{v}}\rho\dot{\varepsilon} \tag{15}$$

where f_{v} represents the DRV coefficient.

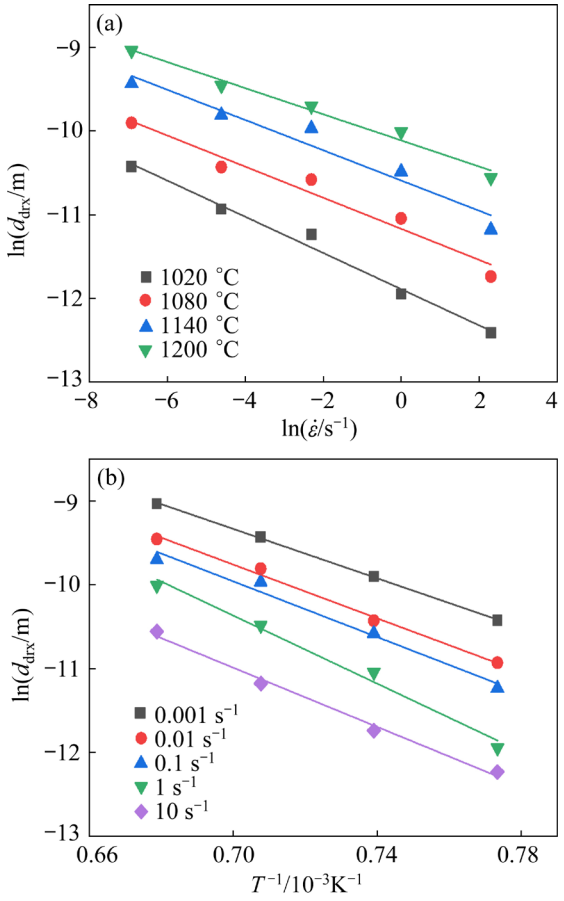

Fig. 9 Fitting lines of $\ln d_{\mathrm{drx}}-\ln\dot{\varepsilon}$ (a) and $\ln d_{\mathrm{drx}}-1/T$ (b) for GH4698 superalloy

(3) Modeling $\dot{\rho}_{\mathrm{DRX}}$

GH4698 superalloy is a metallic material with low stacking fault energy. It signifies that the dislocation climb and dislocation cross-slip are difficult to activate in such metallic materials, and DRV proceeds slowly [37]. The dislocation annihilation caused by DRV is hard to balance with the dislocation multiplication, and dislocations continue to multiply. As soon as the local dislocation density outstrips the critical dislocation density for DRX, DRX is activated, and dislocation annihilation quickly takes place, promoting the

decrease of dislocation density. The rate of dislocation density evolution induced by DRX gives [44]

$$\dot{\rho}_{\mathrm{DRX}} = f_{\mathrm{x}} X \rho \dot{\varepsilon} \tag{16}$$

where f_{x} stands for the DRX coefficient. The critical dislocation density for DRX (ρ_{cr}) is represented as [45]

$$\rho_{\mathrm{cr}} = \left(\frac{20\gamma_{\mathrm{G}} \dot{\varepsilon}}{3b\Lambda_0 M_{\mathrm{bm}} \lambda^2} \right)^{1/3} \tag{17}$$

where γ_{G} represents the grain boundary energy, Λ_0 stands for the initial MFP of dislocation, M_{bm} signifies the grain boundary mobility, and λ stands for the dislocation line energy. These four parameters are given by [46]

$$\gamma_{\mathrm{G}} = \frac{\mu b \theta_{\mathrm{m}}}{4\pi(1-\nu)} \tag{18}$$

$$\Lambda_0 = k_{\mathrm{d}} b \left(\frac{\mu}{\sigma_{\mathrm{y}}} \right)^m \tag{19}$$

$$M_{\mathrm{bm}} = \frac{b\delta D_{\mathrm{ob}}}{k_{\mathrm{B}} kT} \exp\left(-\frac{Q_{\mathrm{dif}}}{RT} \right) \tag{20}$$

$$\lambda = \frac{\mu b^2}{2} \tag{21}$$

where θ_{m} represents the misorientation of HAGB and equals 15°; ν stands for the Poisson ratio and takes 0.33; k_{d} and m signify the material constants and take 10 and 1.33, respectively; δ and D_{ob} stand for the average thickness of grain boundary and grain boundary diffusion coefficient, respectively, and their product δD_{ob} equals 3.5×10^{-15} m^3/s; Q_{dif} signifies the boundary diffusion activation energy and takes 115 kJ/mol; k_{B} signifies Boltzmann constant and equals 1.381×10^{-23} J/K [45].

3.3.3 Modeling σ_{g}

In Hall−Petch equation, the relationship between the grain size and stress under room temperature is described [47]. Generally, metals with fine grains possess high strength. However, the metals with fine grains exhibit the opposite characteristics during high-temperature deformation. Furthermore, the grain size is strongly affected by the DRX fraction. Consequently, the stress for the evolution of grain size can be assumed as

$$\sigma_{\mathrm{g}} = f_{\mathrm{g}} X d^{-1/2} \tag{22}$$

where f_{g} stands for the grain size evolution coefficient.

3.3.4 Definition and solution of material parameters

In the established model, six key parameters need to be determined, namely WH coefficient f_{w}, DRV coefficient f_{v}, DRX coefficient f_{x}, grain size evolution coefficient f_{g}, DRX fraction coefficient f_{k} and DRX fraction index f_{d}. It is assumed that DRX fraction coefficient f_{k} is a material constant, and the other five parameters comply with the Arrhenius-type relation, which are expressed as [48]

$$f_{\mathrm{w}} = A_{\mathrm{w}} \dot{\varepsilon}^{n_{\mathrm{w}}} \exp\left(\frac{Q_{\mathrm{w}}}{RT} \right) \tag{23}$$

$$f_{\mathrm{v}} = A_{\mathrm{v}} \dot{\varepsilon}^{n_{\mathrm{v}}} \exp\left(\frac{Q_{\mathrm{v}}}{RT} \right) \tag{24}$$

$$f_{\mathrm{x}} = A_{\mathrm{x}} \dot{\varepsilon}^{n_{\mathrm{x}}} \exp\left(\frac{Q_{\mathrm{x}}}{RT} \right) \tag{25}$$

$$f_{\mathrm{g}} = A_{\mathrm{g}} \dot{\varepsilon}^{n_{\mathrm{g}}} \exp\left(\frac{Q_{\mathrm{g}}}{RT} \right) \tag{26}$$

$$f_{\mathrm{d}} = A_{\mathrm{d}} \dot{\varepsilon}^{n_{\mathrm{d}}} \exp\left(\frac{Q_{\mathrm{d}}}{RT} \right) \tag{27}$$

where A_{w}, n_{w}, Q_{w}, A_{v}, n_{v}, Q_{v}, A_{x}, n_{x}, Q_{x}, A_{g}, n_{g}, Q_{g}, A_{d}, n_{d} and Q_{d} are the material constants.

In order to achieve high prediction accuracy, a function with sixteen independent variables written by the implicit iterative method is introduced as

$$F(A_{\mathrm{w}}, n_{\mathrm{w}}, Q_{\mathrm{w}}, A_{\mathrm{v}}, n_{\mathrm{v}}, Q_{\mathrm{v}}, A_{\mathrm{x}}, n_{\mathrm{x}}, Q_{\mathrm{x}}, A_{\mathrm{g}}, n_{\mathrm{g}}, Q_{\mathrm{g}}, A_{\mathrm{d}}, n_{\mathrm{d}}, Q_{\mathrm{d}}, f_{\mathrm{k}}) = \sum_{i=1}^{N} \left(\sigma_{\mathrm{P}i} - \sigma_{\mathrm{M}i} \right)^2 \tag{28}$$

where N signifies the number of data spots, i represents the index of each-data spot ranging from 1 to N, $\sigma_{\mathrm{P}i}$ signifies the ith predicted stress, and $\sigma_{\mathrm{M}i}$ signifies the ith measured stress. In order to minimize the function value, the values of sixteen variables are optimized through the Fminsearch method in MATLAB software. Table 1 presents the optimal values of material parameters.

3.3.5 Validation of improved constitutive model

Figure 10 compares the measured stresses and predicted stresses under different parameters. Except for those under high deformation temperatures (1140 and 1200 °C) and high strain rates (1 and 10 s^{-1}), the predicted stresses correlate well with the measured stresses. Under high deformation temperatures, the temperature rising caused by high strain rates declines, as demonstrated

Table 1 Optimal values of material parameters

Material parameter	Value	Material parameter	Value
A_w	48.67	Q_x/(kJ·mol^{-1})	−16.61
n_w	−0.2496	A_g	-4.814×10^{-3}
Q_w/(kJ·mol^{-1})	−1.723	n_g	-2.027×10^{-3}
A_v	1.846×10^{3}	Q_g/(kJ·mol^{-1})	40.52
n_v	7.716×10^{-3}	A_d	3.788×10^{-4}
Q_v/(kJ·mol^{-1})	−49.79	n_d	−0.1355
A_x	29.75	Q_d/(kJ·mol^{-1})	90.64
n_x	0.3410	f_k	0.9939

in Fig. 4. This makes the dislocation annihilation from DRX difficult to counteract the dislocation multiplication. On the macro level, it is manifested as continuous hardening or discontinuous softening characteristics. Consequently, the improved unified dislocation density-based constitutive model cannot well predict these characteristics.

In order to evaluate the prediction accuracy, the correlation coefficient (CC), average absolute relative error (AARE) as well as root mean square error (RMSE) are introduced, and the calculation formulas are given as

$$\mathrm{CC}=\frac{\sum_{i=1}^{N}(x_{\mathrm{P}i}-\overline{x}_{\mathrm{P}})(x_{\mathrm{M}i}-\overline{x}_{\mathrm{M}})}{\sqrt{\sum_{i=1}^{N}(x_{\mathrm{P}i}-\overline{x}_{\mathrm{P}})^2\sum_{i=1}^{N}(x_{\mathrm{M}i}-\overline{x}_{\mathrm{M}})^2}} \tag{29}$$

$$\mathrm{AARE}=\frac{1}{N}\sum_{i=1}^{N}\left|\frac{x_{\mathrm{P}i}-x_{\mathrm{M}i}}{x_{\mathrm{M}i}}\right|\times100\% \tag{30}$$

$$\mathrm{RMSE}=\sqrt{\frac{1}{N}\sum_{i=1}^{N}\left(x_{\mathrm{P}i}-x_{\mathrm{M}i}\right)^2} \tag{31}$$

where $x_{\mathrm{M}i}$ and $x_{\mathrm{P}i}$ stand for the ith measured data and ith predicted data, respectively; $\overline{x}_{\mathrm{M}}$ and $\overline{x}_{\mathrm{P}}$ stand for the average values of the measured data and the predicted data, respectively. The comparison between the predicted and measured stresses is represented in Fig. 11. Based on Eqs. (29), (30) and (31), the CC, AARE and RMSE are calculated as 0.994, 7.32% and 10.8 MPa, respectively. The statistical results and Fig. 11 indicate that the

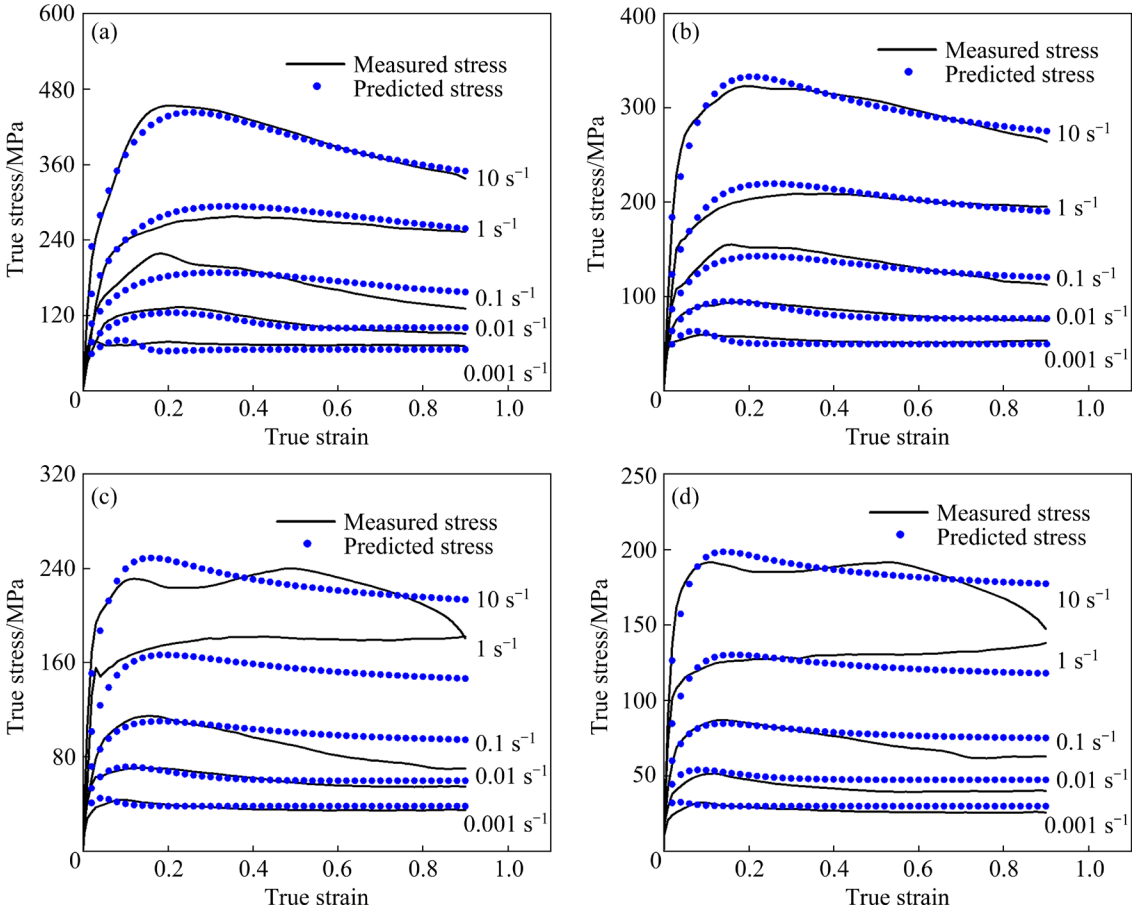

Fig. 10 Measured stresses and predicted stresses of GH4698 superalloy under different deformation temperatures: (a) 1020 °C; (b) 1080 °C; (c) 1140 °C; (d) 1200 °C

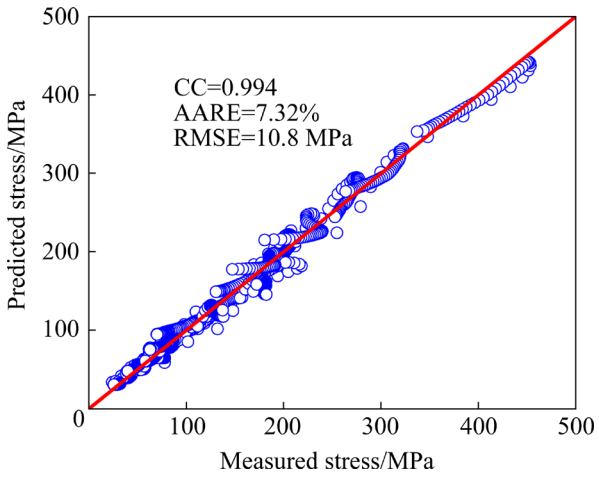

Fig. 11 Comparison between measured stresses and predicted stresses of GH4698 superalloy

established model exhibits high prediction accuracy for the high-temperature deformation behaviors of GH4698 superalloy.

Substituting the values of f_k and f_d in Table 1 into Eq. (12), the DRX kinetics model is obtained, as depicted in Fig. 12. It is noticeable that under a given strain rate, the DRX fraction rises with the increase of deformation temperature. Furthermore, under low deformation temperatures (1020 and 1080 °C), the DRX fraction decreases with the strain rate rising from 0.001 to 1 s^{-1}, and the DRX fraction increases with the strain rate rising to 10 s^{-1}, which has been confirmed by the EBSD analysis. However, under high deformation temperatures (1140 and 1200 °C), the DRX fraction declines with the increase of strain rate. Under high deformation temperatures, the temperature rising caused by high strain rates declines greatly (Fig. 4), and its promotion effect on DRX decreases. It results in the fact that the DRX fraction under the strain rate of 10 s^{-1} is reduced, compared to that under the strain rate of 1 s^{-1}.

Table 2 lists the comparison of measured and predicted DRX fractions under different deformation parameters. The absolute values of relative error are less than 3% except for the one under the deformation temperature of 1020 °C and strain rate of 1 s^{-1}. Besides, the CC is calculated as 0.976. It demonstrates that the DRX kinetics model presents a good capability in predicting the DRX fraction of GH4698 superalloy.

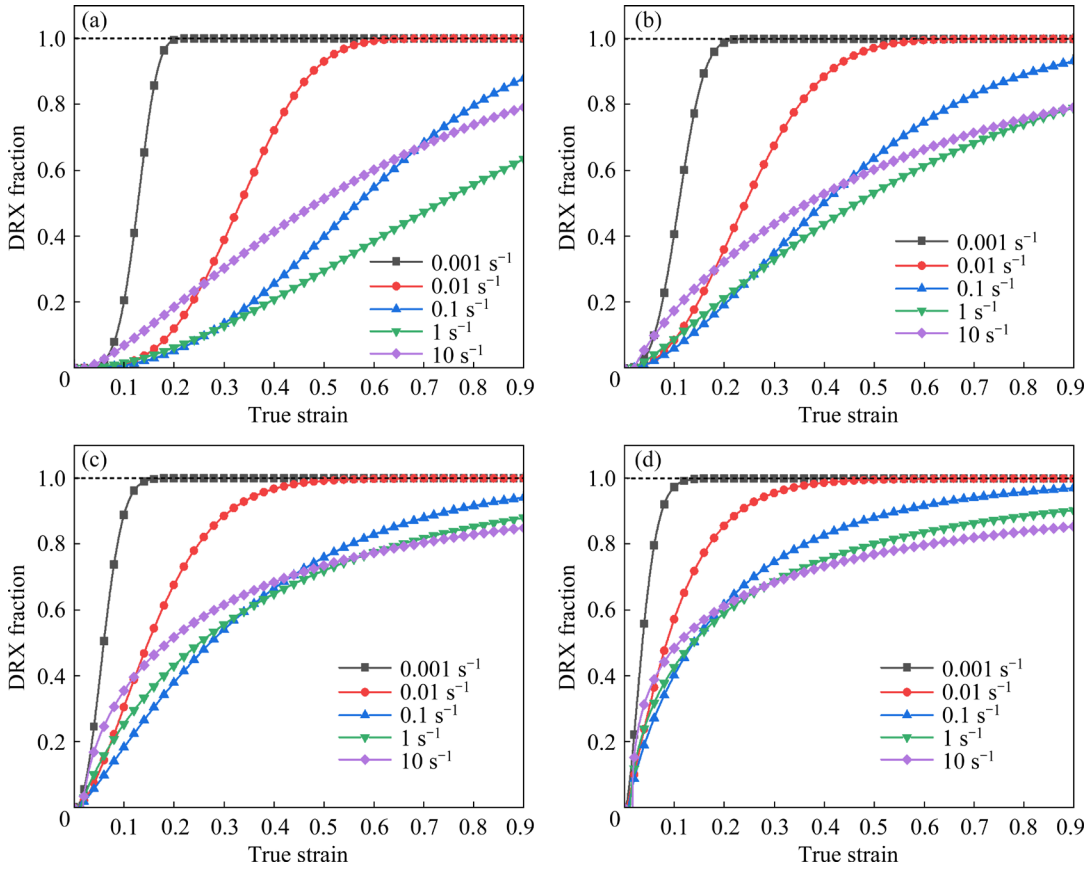

Fig. 12 DRX fractions of GH4698 superalloy under different deformation temperatures: (a) 1020 °C; (b) 1080 °C; (c) 1140 °C; (d) 1200 °C

Table 2 Comparison of measured and predicted DRX fractions under different deformation parameters

Deformation temperature/°C	Deformation strain rate/s^{-1}	Measured DRX fraction/%	Predicted DRX fraction/%	Relative error/%	Correlation coefficient
1020	0.01	97.2	100.0	2.88	0.976
1020	0.1	90.3	87.9	−2.66	
1020	1	56.2	63.3	12.63	
1020	10	81.3	79.1	−2.71	
1080	0.1	91.8	93.1	1.42	
1140	0.1	96.2	94.2	−2.08	

4 Conclusions

(1) The flow stress of GH4698 superalloy is significantly influenced by deformation parameters. With the deformation temperature decreasing or the strain rate increasing, the flow stress increases. Furthermore, the flow stress presents the prominent softening characteristics under the strain rate of 10 s^{-1} due to the great temperature rising under high strain rate.

(2) As the deformation temperature increases or the strain rate decreases, the DRX fraction rises. But, the DRX fraction rises as the strain rate increases from 1 to 10 s^{-1}, because the rapid dislocation multiplication and deformation heat facilitate the nucleation of DRXed grains.

(3) Discontinuous DRX nucleation is the dominant DRX nucleation mechanism. Under low strain rate, continuous DRX nucleation occurs within the deformed grains. Under high strain rate, the time for the migration of LAGBs and the formation of subgrains is insufficient, leading to the slow development of continuous DRX nucleation.

(4) The improved unified dislocation density-based model incorporating DRX effect is established. The CC, AARE and RMSE between the measured and predicted stresses are calculated as 0.994, 7.32% and 10.8 MPa, respectively. Additionally, the CC between the measured and predicted DRX fraction is calculated as 0.976. The developed model exhibits a good capability in predicting the high-temperature deformation and DRX behaviors of GH4698 superalloy.

CRediT authorship contribution statement

Pei-zhi YAN: Conceptualization, Methodology, Investigation, Writing − Original draft, Writing − Review & editing; **Dong-xu WEN:** Methodology, Writing − Review & editing, Funding, Supervision; **Qi-feng DING:** Investigation; **Liang HUANG:** Resources, Funding; **Xiao-li YANG:** Resources, Funding; **Zhi-cheng ZHANG:** Resources, Funding; **Jian-jun LI:** Resources, Funding, Supervision.

Declaration of competing interest

The authors declare that they have no known competing financial interests or personal relationships that could have appeared to influence the work reported in this paper.

Acknowledgments

This study was financially supported by the National Natural Science Foundation of China (No. 52375337), the Key Research and Development Program of Hubei Province, China (No. 2022BAA024), and the Fundamental Research Funds for the Central Universities, China (No. 2019kfyXJJS001).

References

[1] LI Fang, YUAN Ding-ling, CHEN Kang-hua, CHEN Song-yi, LI Li. A novel creep model with synergetic Orowan bypassing and climbing mechanisms in nickel-base superalloys [J]. Transactions of Nonferrous Metals Society of China, 2024, 34: 1167−1177.

[2] THESKA F, STREET S R, LISON-PICK M, PRIMIG S. Grain boundary microstructure−property relationships in the cast & wrought Ni-based superalloy René 41 with boron and carbon additions [J]. Acta Materialia, 2023, 258: 119235.

[3] ZENG Quan, WANG Ke-lu, LU Shi-qiang, LU Cui-yuan, WANG Zeng-qiang, ZHOU Tong. Evolution of the microstructure and multi-objective optimization of the tensile properties of GH3625 superalloy by selective laser melting [J]. Journal of Materials Research and Technology, 2023, 24: 8826−8848.

[4] XU Guo-hua, DUAN Ran, WANG Lei, LIU Yang, MENG Fan-qiang. Effect of compositional homogenization on hot workability of Ni-based GH4061 superalloy [J]. Transactions of Nonferrous Metals Society of China, 2023, 33:

1792−1802.

[5] QU Zong-hong, ZHANG Ping-xiang, LAI Yun-jin, WANG Qing-xiang, SONG Jia-ming, LIANG Shu-jin. Influence of powder particle size on the microstructure of a hot isostatically pressed superalloy [J]. Journal of Materials Research and Technology, 2022, 16: 1283−1292.

[6] KUMAR S S S, RAGHU T, BHATTACHARJEE P P, RAO G A, BORAH U. Work hardening characteristics and microstructural evolution during hot deformation of a nickel superalloy at moderate strain rates [J]. Journal of Alloys and Compounds, 2017, 709: 394−409.

[7] WEN Hong-ning, JIN Jun-song, TANG Xue-feng, WANG Xin-yun, YANG He-yang, ZHANG Yi-ding, DENG Lei, GONG Pan, WEI Qing-song, HE Ying-jie, GUO Jian-zheng. Systematic analysis of distinct flow characteristics and underlying microstructural evolution mechanisms of a novel fine-grained P/M nickel-based superalloy during isothermal compression [J]. Journal of Materials Science & Technology, 2023, 162: 57−73.

[8] XIE Bing-chao, LI Heng, NING Yong-quan, FU Ming-wang. Discontinuous dynamic recrystallization and nucleation mechanisms associated with 2-, 3- and 4-grain junctions of polycrystalline nickel-based superalloys [J]. Materials & Design, 2023, 231: 112041.

[9] ZHANG Jie-ke, CAO Yu, GONG Yu-hao, XIAO Jun, ZHU Yu-long, LUO Rui, HE Qu-bo, LIU Qing. Revealing hot deformation behavior of Inconel X-750 superalloy: A novel hot processing map coupled with grain boundary engineering [J]. Journal of Materials Research and Technology, 2023, 25: 1245−1262.

[10] ZHU Yu-long, CAO Yu, HE Qu-bo, ZHANG Jie-ke, LUO Rui, DI Hong-shuang, HUANG Guang-jie, LIU Qing. Three-dimensional hot processing map of a nickel-based superalloy (Alloy 925) established by modified artificial neural network model [J]. Intermetallics, 2022, 141: 107433.

[11] YAN Pei-zhi, WEN Dong-xu, LIU Yang, HUANG Liang, YANG Xiao-li, ZHANG Zhi-cheng, XU Fu-ze, LI Jian-jun. Evolution of microstructure and δ phase in an aging-treated nickel-based superalloy during hot compression [J]. Materials Characterization, 2023, 200: 112876.

[12] LUO Jiao, LI Xiang-yang, LI Cong, LI Miao-quan. Effect of processing parameters on flow behaviors and microstructure during high temperature deformation of GH4586 superalloy [J]. Journal of Central South University, 2021, 28: 338−350.

[13] SHOKRY A, GOWID S, YOUSSEF S S. Modeling the flow behavior of Haynes 214 superalloy during hot deformation using mathematical and artificial intelligence-based models [J]. Materials Today Communications, 2022, 33: 104326.

[14] CHRISTOPHER J, NANDAGOPAL M, PALAPARTI D P R, PRASAD REDDY G V, ALBERT S K. Saturation stress based models and their applicability to tensile flow behaviour of superalloy 617M [J]. International Journal of Pressure Vessels and Piping, 2021, 192: 104419.

[15] CHEN Xiao-min, NIE Liao-yuan, HU Hong-wei, LIN Yong-cheng, LIU Yan-xing, WU Zi-lang, ZHOU Xiao-jie, ZHANG Jian, LU Xian-zheng. High-temperature deformation characteristics and constitutive models of Inconel 625 superalloy [J]. Materials Today Communications, 2022, 32: 103855.

[16] ZHU Yu-long, CAO Yu, LIU Cun-jian, LUO Rui, LI Na, SHU Gang, HUANG Guang-jie, LIU Qing. Dynamic behavior and modified artificial neural network model for predicting flow stress during hot deformation of Alloy 925 [J]. Materials Today Communications, 2020, 25: 101329.

[17] WEN Hong-ning, JIN Jun-song, TANG Xue-feng, WANG Xin-yun, YANG He-yang, ZHANG Yi-ding, ZHANG Mao, DENG Lei, WEI Qing-song, CHEN Jun-zhi, MA Xiang-dong, GUO Jian-zheng. Machine learning-assisted constitutive modeling of a novel powder metallurgy superalloy [J]. International Journal of Mechanical Sciences, 2023, 260: 108654.

[18] CHEN Xiao-min, NIE Liao-yuan, HU Hong-wei, LIN Yong-cheng, ZHANG Jian, ZHOU Xiao-jie, LU Xian-zheng, CHEN Jian, LIU Yan-xing. Investigation on the fracture mechanism and constitutive relations of a typical Ni-based superalloy [J]. Materials Today Communications, 2023, 35: 105612.

[19] TANG Xue-feng, WANG Bao-yu, ZHANG Ning, HUO Yuan-ming, ZHOU Jing. Modeling of microstructural evolution and flow behavior of superalloy IN718 using physically based internal state variables [J]. Rare Metals, 2022, 41: 2759−2766.

[20] HE Dao-guang, YAN Xin-tao, LIN Yong-cheng, ZHANG Song, CHEN Zi-Jian. Microstructure evolution and constitutive model for a Ni−Mo−Cr base alloy in double-stages hot compression with step-strain rates [J]. Materials Characterization, 2022, 194: 112385.

[21] GUO Zi-xu, SONG Zi-yuan, LIU Hao-hao, HU Dai-jun, HUANG Da-wei, YAN Xiao-jun, YAN Wen-tao. A dislocation-based damage-coupled constitutive model for single crystal superalloy: Unveiling the effect of secondary orientation on creep life of circular hole [J]. International Journal of Plasticity, 2024, 173: 103874.

[22] HE Dao-guang, CHEN Xiao-yang, LIN Yong-cheng. The improved physically-mechanism constitutive model for a Ni−Mo−Cr-based superalloy with the pre-precipitation of μ phase in hot forming [J]. Journal of Alloys and Compounds, 2024, 997: 174934.

[23] LI Hai-zhu, LIU Xin-gang, ZHANG Wen-wen, LIU Peng-wei, GUO Shu-ling, QIN He-yong, TIAN Qiang. Microstructure evolution and dynamic recrystallization mechanism during thermal deformation of GH4698 superalloy [J]. Journal of Materials Science, 2022, 57: 2969−2987.

[24] LI Hai-zhu, LIU Xin-gang, WANG Shuai-jie, ZHANG Wen-wen, KE Yu-jiao, GUO Ying, QIN He-yong, TIAN Qiang. An evaluation of optimized grain boundary character distribution in hot-worked GH4698 superalloy [J]. Journal of Materials Science, 2023, 58: 1382−1402.

[25] ZHANG Peng, HU Chao, ZHU Qiang, DING Chao-gang, QIN He-yong. Hot compression deformation and constitutive modeling of GH4698 alloy [J]. Materials & Design, 2015, 65:

1153−1160.

[26] CHEN Rong-chuang, XIAO Hai-feng, WANG Min, LI Jian-jun. Flow behavior and hot processing map of GH4698 for isothermal compression process [J]. Processes, 2019, 7: 491.

[27] CHEN Xiao-min, NING Meng-tao, HU Hong-wei, LIN Yong-cheng, ZHOU Xiao-jie, ZHANG Jian, LU Xian-zheng, CHEN Jian, LIU Yan-xing. Characterization of hot deformation behavior and optimization of hot workability for GH4698 superalloy [J]. Materials Characterization, 2023, 201: 112916.

[28] SONG Yao-hui, LI Yu-gui, LI Hua-ying, ZHAO Guang-hui, CAI Zhi-hui, SUN Ming-xu. Hot deformation and recrystallization behavior of a new nickel-base superalloy for ultra-supercritical applications [J]. Journal of Materials Research and Technology, 2022, 19: 4308−4324.

[29] ZHANG Zhi-xin, FAN Jiang-kun, TANG Bin, KOU Hong-chao, WANG Jian, CHEN Zhi-yong, LI Jin-shan. Microstructure/texture evolution maps to optimize hot deformation process of near-α titanium alloy [J]. Progress in Natural Science: Materials International, 2020, 30: 86−93.

[30] QU Zong-hong, ZHANG Ping-xiang, LIANG Shu-jin, LAI Yun-jin, WANG Jun, FAN Jiang-kun, BAI Rui-min. Flow behavior and dynamic recrystallization of hot isostatically pressed EP741NP superalloy [J]. Journal of Materials Research and Technology, 2022, 18: 2112−2124.

[31] ZHOU Xiong, LE Qi-chi, HU Cheng-lu, LI Dan-dan, WANG Tong, LIAO Qi-yu, GUO Rui-zhen, LIU Chun-ming, LIU Xiao-tao. Study on the hot deformation behavior of a novel multi-element synergistic strengthening Mg−Al−Ca−Mn−Zn−Sn alloy [J]. Journal of Alloys and Compounds, 2023, 953: 170156.

[32] MIRZADEH H. Grain refinement of magnesium alloys by dynamic recrystallization (DRX): A review [J]. Journal of Materials Research and Technology, 2023, 25: 7050−7077.

[33] TAN Li-ming, LI Yun-ping, LIU Feng, NIE Yan, JIANG Liang. Microstructure evolutions of a powder metallurgy superalloy during high-strain-rate deformation [J]. Journal of Alloys and Compounds, 2019, 789: 506−517.

[34] ZHANG Jian-yang, XU Bin, TARIQ N H, SUN Ming-yue, LI Dian-zhong, LI Yi-yi. Microstructure evolutions and interfacial bonding behavior of Ni-based superalloys during solid state plastic deformation bonding [J]. Journal of Materials Science & Technology, 2020, 46: 1−11.

[35] WANG Yan-jiang, JIA Zhi, GAO Ze-xi, LIU De-xue. Continuous dynamic recrystallization nucleation mechanism and annealing twin evolution with respect to grain growth in a nickel-based superalloy [J]. Journal of Central South University, 2023, 30: 49−60.

[36] PRAVEEN C, CHRISTOPHER J, GANESAN V, PRASAD REDDY G V, CHOUDHARY B K. Dislocation density based modeling of three-stage work hardening behaviour of type 316LN SS with varying nitrogen content and its finite element implementation for different notch radii [J]. Materials Chemistry and Physics, 2020, 241: 122342.

[37] YANG Wen-chao, QU Peng-fei, LIU Chen, CAO Kai-li, QIN Jia-run, SU Hai-jun, ZHANG Jun, REN Cui-dong, LIU Lin. Temperature dependence of compressive behavior and deformation microstructure of a Ni-based single crystal superalloy with low stacking fault energy [J]. Transactions of Nonferrous Metals Society of China, 2023, 33: 157−167.

[38] HE Yi, LI Wei-guo, PI Wen-li, YANG Meng-qing, DONG Pan, ZHANG Zhi-qing. Physics-based model to predict yield strength of single-phase FCC high-entropy alloys over wide temperature range [J]. Transactions of Nonferrous Metals Society of China, 2023, 33: 3770−3782.

[39] CHEN Zi-jian, LIN Yong-cheng, HE Dao-guang, LOU Yu-ming, CHEN Ming-song. A unified dislocation density-based model for an aged polycrystalline Ni-based superalloy considering the coupled effects of complicate deformation mechanisms and initial δ phase [J]. Materials Science and Engineering: A, 2021, 827: 142062.

[40] FUKUHARA M, SANPEI A. Elastic moduli and internal frictions of Inconel 718 and Ti−6Al−4V as a function of temperature [J]. Journal of Materials Science Letters, 1993, 12: 1122−1124.

[41] COLLINS D M, STONE H J. A modelling approach to yield strength optimisation in a nickel-base superalloy [J]. International Journal of Plasticity, 2014, 54: 96−112.

[42] MECKING H, KOCKS U F. Kinetics of flow and strain-hardening [J]. Acta Metallurgica, 1981, 29: 1865−1875. (in French)

[43] LIU Guo-wang, MAO Chun-liang, DING Ran, YU Li-ming, LIU Chen-xi, LIU Yong-chang. The kinetics of dynamic recrystallization and construction of constitutive modeling of RAFM steel in the hot deformation process [J]. Journal of Nuclear Materials, 2021, 557: 153285.

[44] GALINDO-NAVA E I, SIETSMA J, RIVERA-DÍAZ-DEL-CASTILLO P E J. Dislocation annihilation in plastic deformation: II. Kocks−Mecking analysis [J]. Acta Materialia, 2012, 60: 2615−2624.

[45] ROBERTS W, AHLBLOM B. A nucleation criterion for dynamic recrystallization during hot working [J]. Acta Materialia, 1978, 26: 801−813. (in French)

[46] DERBY B. The dependence of grain size on stress during dynamic recrystallisation [J]. Acta Metallurgica et Materialia, 1991, 39: 955−962. (in French)

[47] CHEN Cai, HAN Dong-sheng, SONG Yu-tao, WANG Ming-chuan, LI Yu-sheng, XU Shun, YANG Sen, LIU Ji-zi. Effect of grain size and temperature on deformation mechanism of commercially pure titanium [J]. Transactions of Nonferrous Metals Society of China, 2023, 33: 3332−3347.

[48] WEN Dong-xu, ZHANG Meng, XIONG Yi-bo, WANG Wen-hai, LI Jian-jun. Constitutive modeling hot tensile behavior of Ti6Al4V alloy by considering phase transformation and damage mechanisms [J]. Materials Science and Engineering: A, 2024, 890: 145887.

GH4698 合金高温变形和动态再结晶行为的改进型位错密度统一本构模型

颜佩智[1]，温东旭[1]，丁琦峰[1]，黄 亮[1]，杨晓利[2]，张志成[2]，李建军[1,3]

1. 华中科技大学 材料科学与工程学院 材料成形与模具技术全国重点实验室，武汉 430074；
2. 大冶特殊钢有限公司，黄石 435001；
3. 湖北黄石科创模具技术研究院有限公司，黄石 435007

摘 要：通过热压缩试验研究了 GH4698 合金的高温变形和动态再结晶行为，并建立了改进型位错密度统一本构模型。结果表明，随着温度的降低或应变速率的增加，流变应力逐渐增加，动态再结晶分数降低。然而，当应变速率从 1 s^{-1} 升至 10 s^{-1} 时，位错的快速增殖和变形热的产生促进了动态再结晶形核，从而提高了动态再结晶分数。不连续动态再结晶形核是主要的动态再结晶形核机制，连续动态再结晶形核主要发生在低应变速率条件下。对于所建立的改进型位错密度统一本构模型，流变应力的实测值与预测值之间的相关系数、平均绝对相对误差和均方根误差分别为 0.994、7.32%和 10.8 MPa。同时，动态再结晶分数的实测值和预测值之间的相关系数为 0.976。这表明所建立的模型在预测 GH4698 合金的高温变形和动态再结晶行为方面具有较高的准确性。

关键词：镍基高温合金；本构模型；高温变形；动态再结晶

(Edited by Wei-ping CHEN)